Supplement of Earth Surf. Dynam., 9, 795–822, 2021
https://doi.org/10.5194/esurf-9-795-2021-supplement

Earth Surface Dynamics
Open Access
EGU

Supplement of

Tectonically and climatically driven mountain-hopping erosion in central Guatemala from detrital ^{10}Be and river profile analysis

Gilles Brocard et al.

Correspondence to: Gilles Brocard (gilles.brocard@mom.fr)

Supplement

Content:

Supplement 1: $^{40}Ar/^{39}Ar$ radiometric dating.
Supplement 2: Terrestrial ^{10}Be measurements and conversion to erosion rates
Supplement 3: River profile segmentation
Supplement 4: River segments and knickpoints analysis

Supplement 1. *$^{40}Ar/^{39}Ar$ isotopic dating*

The crushed whole-rock samples were irradiated with standards in 3 separate irradiations at 0.5, 3, and 5 MWh, respectively, in the central thimble position of the USGS TRIGA reactor (Dalrymple et al., 1981), while being rotated at 1 rpm. Following irradiation, the samples and standards were loaded to a stainless steel sample holder with tweezers and then placed into a laser chamber with an externally pumped ZnSe window. The volume of the mostly stainless steel vacuum extraction line, including a cryogenic trap operated at -130°C and two SAES™ GP50 getters (one operated at room temperature, one at 2.2A), is ~450 cm^3. A combination of turbo molecular pumps and ion pumps maintains steady pressures at < 1.33 10^{-7} Pa within the extraction line. Samples were incrementally heated in steps of 90 seconds, by controlled power output of a 50W CO_2 laser equipped with a beam-homogenizing lens, which results in a uniform energy distribution over the entire sample surface. Any sample gas that was released during laser heating was exposed to the cryogenic trap and further purified for an additional 120 seconds by exposure to both the cryogenic trap and the SAES getters. The sample gas was expanded into a Thermo Scientific ARGUS VI™ mass spectrometer where argon isotopes were analyzed simultaneously using four faraday detectors (^{40}Ar, ^{39}Ar, ^{38}Ar, ^{37}Ar) and an ion counter (^{36}Ar). Detector calibration was carried out using a fixed reference voltage on the faraday detectors. The ion counter was calibrated relative to the faraday detectors by regular air pipette measurements, and the detector discrimination was monitored by the $^{40}Ar/^{39}Ar$ ratios of Fish Canyon sanidine measurements. Following 10 minutes of data acquisition, time zero intercepts were fit to the data (using parabolic and/or linear best fits) and corrected for backgrounds, detector inter-calibrations, and nucleogenic interferences. The computer program Mass Spec (A. Deino, Berkeley Geochronology Center) was used for data acquisition, age calculations, and plotting (Fig.S1-1). The $^{40}Ar/^{39}Ar$ ages reported in Table S1-2 are calculated assuming an age of 28.201 ± 0.046 Ma for the Fish Canyon sanidine (Kuiper et al., 2008), using the decay constants of Min et al. (2000), and an atmospheric $^{40}Ar/^{36}Ar$ of 298.56 ± 0.31 (Lee et al., 2010). Laser fusion of more than ten individual Fish Canyon Tuff sanidine crystals at each closely monitored position within the irradiation package resulted in neutron flux ratios reproducible to ≤ 0.25% (2σ). Isotopic production ratios were determined from irradiated CaF_2 and KCl salts. For this study the following values were measured: $(^{36}Ar/^{37}Ar)Ca = (2.4 \pm 0.05)10^{-4}$; $(^{39}Ar/^{37}Ar)Ca = (6.59 \pm 0.10)10^{-4}$; and $(^{38}Ar/^{39}Ar)K = (1.29 \pm 0.03)10^{-2}$. Cadmium shielding during irradiation prevented any measurable $(^{40}Ar/^{39}Ar)K$. For the calculation of the plateau ages we required three or more consecutive heating steps that released ≥ 50% of the total ^{39}Ar and also had statistically (2σ) indistinguishable $^{40}Ar/^{39}Ar$ ages.

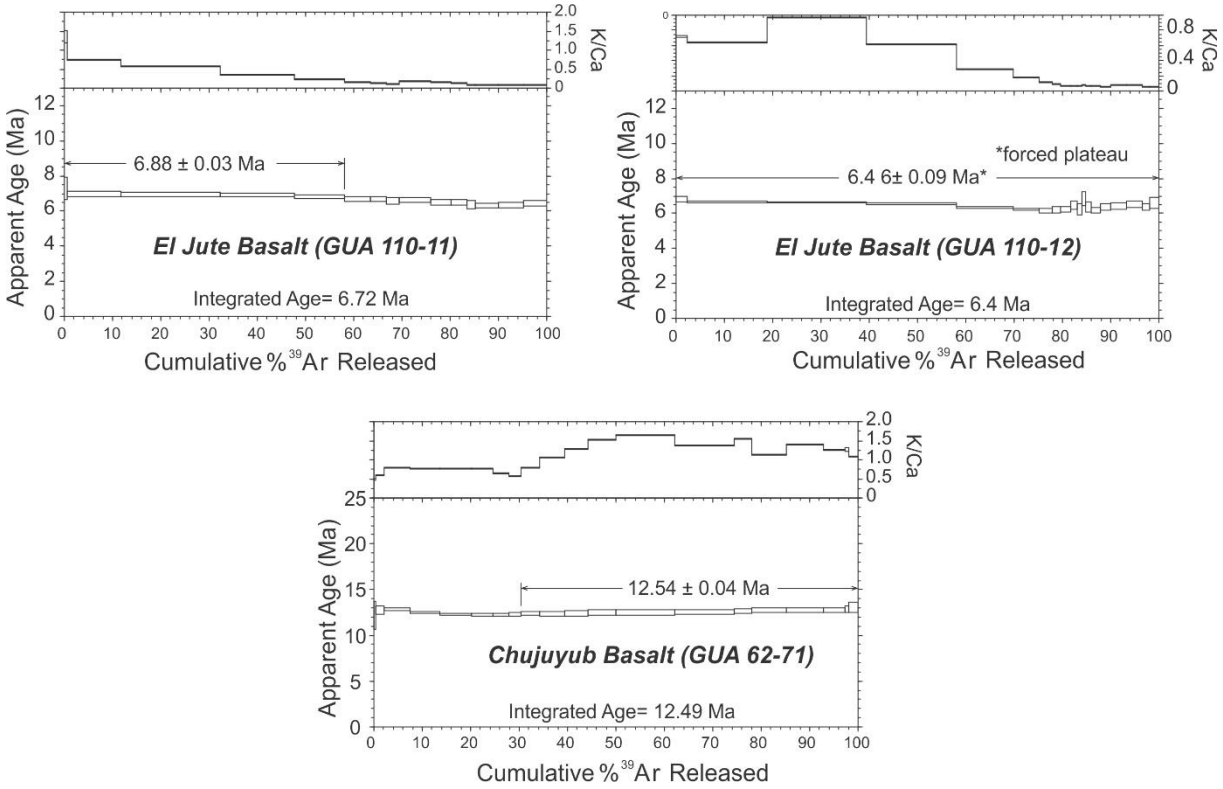

Figure S1-1. Heating step releases and statistics for the calculation of whole rock basalt $^{40}Ar/^{39}Ar$ ages.

Table SI-y. $^{40}Ar/^{39}Ar$ results

CO_2 laser	Relative Isotopic Abundances (x 10^{-13}A)										Derived Results						
Power	^{40}Ar		^{39}Ar		^{38}Ar		^{37}Ar		^{36}Ar		^{39}Ar Mol	^{39}Ar %	Ca/K		% ^{40}Ar*	Age (Ma)	
(Watts)	±1σ		±1σ		±1σ		±1σ		±1σ		∞ 10^{-16}	of total	±1σ			±2σ	
GUA 62-71 , whole rock, J ± 1σ = 1.1085 ± 0.001 (x10-^{3}). Location: 91.04° E, 15.10°N																	
0.9	46655.91	17.05	825.84	15.73	51.42	6.18	465.42	5.24	140.68	0.56	4.0	0.4	2.098	0.045	11.0	**12.17**	0.76
1.2	75017.09	23.44	3309.56	15.93	69.89	6.52	1522.25	5.29	181.79	0.52	16.2	1.8	1.713	0.010	28.7	**12.68**	0.24
1.5	98250.87	25.33	9999.04	18.18	139.19	6.31	3413.50	6.01	111.91	0.43	49.0	5.3	1.271	0.003	66.8	**12.81**	0.07
1.8	92109.22	27.23	11596.99	18.16	154.17	6.45	4045.85	6.11	63.62	0.34	56.8	6.2	1.300	0.003	80.2	**12.43**	0.05
2.1	105457.00	30.11	12412.77	19.07	165.06	6.24	4296.59	5.95	95.42	0.40	60.8	6.6	1.290	0.003	73.8	12.24	0.05
2.3	77517.56	23.44	8411.71	17.05	124.33	6.18	2936.32	5.73	86.14	0.40	41.2	4.5	1.301	0.004	67.7	12.17	0.07
2.5	61617.95	21.58	6167.51	15.82	66.12	6.18	2571.49	5.33	79.50	0.39	30.2	3.3	1.554	0.005	62.4	12.17	0.08
2.7	51375.51	19.74	4588.29	14.88	87.22	6.38	2166.49	5.79	77.52	0.37	22.5	2.4	1.761	0.007	56.0	12.23	0.10
3.0	99081.15	30.11	7134.81	16.68	131.35	6.24	2423.34	5.96	183.60	0.57	35.0	3.8	1.267	0.004	45.6	12.35	0.12
3.3	152069.10	42.77	9897.57	18.14	182.67	6.05	2518.24	5.53	304.28	0.79	48.5	5.3	0.949	0.003	41.1	12.32	0.14
3.6	147421.90	36.90	9051.87	16.65	182.18	6.45	1890.86	5.54	306.24	0.73	44.4	4.8	0.780	0.003	38.8	12.33	0.15
4.0	178389.50	43.76	10855.54	17.88	229.76	6.18	1927.31	5.19	370.39	0.79	53.2	5.8	0.663	0.002	38.8	12.44	0.15
5.0	363509.80	88.37	22586.24	24.62	440.98	6.32	3680.93	6.13	744.05	1.19	110.7	12.0	0.608	0.001	39.7	12.45	0.14
6.0	351163.20	79.41	23249.66	25.50	428.22	6.39	4523.01	6.13	684.77	1.09	113.9	12.4	0.727	0.001	42.6	12.54	0.13
6.0	103311.40	27.68	6941.79	15.85	132.28	6.04	1202.92	5.34	198.48	0.65	34.0	3.7	0.653	0.003	43.4	12.60	0.13
7.0	196150.70	45.01	13191.02	18.71	270.91	5.91	3083.53	6.13	374.66	0.84	64.7	7.0	0.881	0.002	43.8	12.70	0.13
8.0	221846.80	51.88	14539.20	19.31	293.01	6.11	2744.21	5.95	432.72	0.90	71.3	7.7	0.711	0.002	42.5	12.66	0.13
9.0	120639.10	33.01	8257.42	16.40	195.17	5.76	1769.90	5.73	227.08	0.65	40.5	4.4	0.809	0.003	44.6	12.71	0.13
10.0	21394.51	14.48	1577.50	14.49	83.58	6.03	331.10	5.92	37.47	0.25	7.7	0.8	0.792	0.016	48.5	12.82	0.18
12.0	88021.11	26.28	3332.18	15.29	87.16	6.39	823.69	5.67	223.26	0.61	16.3	1.8	0.933	0.008	25.2	12.97	0.28
Age Plateau =12.54 ± 0.04 Ma (steps 4.0 - 12.0 watts, 100% ^{39}Ar released)																	
GUA 110-11 , El Jute, whole rock, J ± 1σ = 1.1085 ± 0.001 (x10^{-3}). Location: N 14.975 °, W 89.803°																	
0.9	6343.83	12.38	490.28	14.14	0.00	5.78	97.01	5.04	15.32	0.18	2.4	0.7	0.748	0.043	28.8	**7.29**	0.32
1.2	63882.63	21.93	7995.93	16.92	133.81	6.31	2882.06	5.76	121.40	0.47	39.2	11.2	1.363	0.004	44.5	**6.94**	0.07
1.5	100472.40	29.41	14679.32	19.48	247.64	6.04	6674.09	7.15	167.19	0.63	71.9	20.6	1.719	0.003	51.7	**6.92**	0.06
1.8	71591.87	22.85	10970.59	17.92	152.85	5.85	8035.82	7.96	115.47	0.50	53.8	15.4	2.771	0.006	53.9	**6.87**	0.06
2.1	45699.08	19.24	7341.83	16.12	94.90	5.97	8734.57	7.77	72.35	0.33	36.0	10.3	4.502	0.011	55.8	**6.80**	0.05
2.3	22724.28	15.00	3804.11	15.99	35.91	6.10	6300.06	7.13	35.97	0.26	18.6	5.3	6.268	0.026	57.0	**6.67**	0.06
2.5	13569.04	14.21	2357.50	15.17	32.37	6.52	4867.93	6.70	21.07	0.20	11.6	3.3	7.817	0.049	59.0	**6.65**	0.08
2.7	11404.31	13.16	1956.86	15.14	27.25	6.10	4707.41	6.13	18.65	0.19	9.6	2.7	9.109	0.068	57.3	**6.55**	0.09
3.0	32089.96	15.81	4611.48	16.12	78.32	6.10	6950.11	7.42	59.19	0.34	22.6	6.5	5.708	0.020	48.5	**6.60**	0.07
3.3	20247.29	14.21	3049.27	15.25	22.34	6.10	5356.00	6.46	36.85	0.25	14.9	4.3	6.654	0.033	49.8	**6.48**	0.08
3.6	15359.52	14.21	2362.64	14.56	25.92	6.17	4942.23	6.85	27.81	0.23	11.6	3.3	7.927	0.048	50.9	**6.48**	0.08
4.0	7931.50	13.23	1289.55	16.42	33.46	6.45	3850.05	6.31	14.49	0.18	6.3	1.8	11.317	0.139	52.7	**6.35**	0.12
5.0	22077.14	15.81	3342.33	14.50	31.18	5.91	11942.34	9.76	43.98	0.25	16.4	4.7	13.547	0.058	48.5	**6.29**	0.08
6.0	27076.30	15.81	3750.92	15.35	56.37	6.24	13246.17	10.37	57.01	0.33	18.4	5.3	13.392	0.054	44.5	**6.30**	0.08
7.0	24259.69	15.00	3369.67	15.29	65.60	6.31	11752.32	9.70	50.20	0.32	16.5	4.7	13.230	0.059	45.5	**6.43**	0.09
Age Plateau =6.88 ± 0.03 Ma (steps 0.9 - 2.1 watts, 100% ^{39}Ar released)																	
GUA 110-12 , El Jute, whole rock, J ± 1σ = 1.1085 ± 0.001 (x10^{-3}), Location: N 14.975 °, W 89.803°																	
0.9	10389.23	14.34	1931.37	15.14	12.64	5.76	711.89	5.86	12.82	0.16	9.5	2.4	1.399	0.015	64.5	**6.78**	0.08
1.2	54869.72	19.33	13024.21	19.32	203.84	5.98	5340.98	6.84	38.51	0.29	63.8	16.4	1.557	0.003	80.6	**6.64**	0.03
1.5	66997.67	22.01	16332.39	20.80	253.15	6.13	4446.91	6.53	41.83	0.31	80.0	20.6	1.034	0.002	82.5	**6.61**	0.02
1.8	59050.30	22.01	14786.43	19.53	219.99	5.98	6389.84	7.74	36.04	0.28	72.5	18.7	1.642	0.003	83.5	**6.51**	0.02
2.1	35840.46	16.75	9168.86	17.28	118.34	5.76	8307.56	8.00	25.28	0.20	44.9	11.6	3.443	0.007	82.3	**6.30**	0.03
2.3	16460.64	14.34	4253.32	16.06	65.41	5.62	6406.31	7.00	13.03	0.16	20.8	5.4	5.725	0.022	82.0	**6.21**	0.04
2.5	8472.75	13.22	2189.91	15.16	21.19	5.55	4920.40	6.62	7.77	0.16	10.7	2.8	8.542	0.058	80.9	**6.13**	0.06
2.7	5293.31	13.37	1359.72	15.10	16.45	5.69	4271.08	6.37	5.43	0.14	6.7	1.7	11.945	0.128	80.8	**6.17**	0.09
3.0	6828.58	13.59	1736.71	14.09	21.34	5.83	6534.75	7.16	7.56	0.14	8.5	2.2	14.312	0.112	80.5	**6.21**	0.07
3.3	4461.97	12.32	1109.13	15.08	19.06	5.76	4488.93	6.34	4.87	0.14	5.4	1.4	15.398	0.201	81.6	**6.45**	0.12
3.6	2763.87	13.01	685.88	14.45	0.00	5.69	2570.97	5.99	3.19	0.11	3.4	0.9	14.265	0.288	78.6	**6.22**	0.16
4.0	2597.88	12.59	617.35	15.72	11.03	5.83	2304.89	5.90	2.64	0.10	3.0	0.8	14.212	0.346	82.2	**6.79**	0.20
5.0	3652.92	13.22	896.48	15.08	0.00	5.83	3655.89	6.41	4.27	0.12	4.4	1.1	15.528	0.250	79.2	**6.34**	0.14
6.0	6181.84	13.59	1484.47	14.30	13.35	5.34	6221.75	7.16	8.07	0.15	7.3	1.9	15.963	0.148	75.3	**6.16**	0.09
7.0	8639.62	13.37	1745.69	14.03	0.00	5.98	8344.11	8.34	14.04	0.17	8.6	2.2	18.209	0.141	65.3	**6.35**	0.09
8.0	19248.87	13.90	2623.87	14.49	32.40	5.83	8739.79	8.24	40.29	0.25	12.9	3.3	12.782	0.069	44.5	**6.40**	0.09
9.0	18078.51	12.97	2527.48	14.48	25.23	6.17	8201.38	7.90	36.68	0.28	12.4	3.2	12.455	0.070	46.3	**6.50**	0.10
8.0	5892.63	11.81	1347.63	15.10	19.21	6.18	6417.48	6.51	8.27	0.14	6.6	1.7	18.287	0.196	73.7	**6.33**	0.10
9.0	12855.89	13.90	1383.36	15.10	18.35	5.98	6506.37	7.19	30.89	0.26	6.8	1.7	18.066	0.189	36.0	**6.58**	0.16

Table S1-2. Heating step releases and statistics for the calculation of whole rock basalt $^{40}Ar/^{39}Ar$ ages.

Supplement 2. Terrestrial ^{10}Be measurements and conversion to erosion rates

Sediment grain sizes were separated using a phi-scale sieve set. Fractions coarser than 2 mm were crushed and sieved to obtain a 0.25-0.5 mm powder. Quartz isolation, purification and dissolution, ion exchange extraction and precipitation of beryllium were performed following an adaptation of the technique of (Kohl and Nishiizumi 1992). A ^{9}Be carrier (Scharlau BE03450100 carrier batch 2Q2P – 14/10/10) with a measured $^{10}Be/^{9}Be$ ratio of $1.5x10^{-15}$ was added to each sample. Beryllium hydroxide was precipitated at pH 8-9, oxidized to BeO over an open butane-propane flame and mixed with Nb powder. The $^{10}Be/^{9}Be$ ratio was measured by accelerator mass spectrometry (AMS) at PRIME lab, Purdue University. Results were normalized to the 07KNSTD standard (Nishiizumi, Imamura et al. 2007) with an assumed $^{10}Be/^{9}Be$ ratio of 2.79×10^{-11} (Balco 2009). The $^{10}Be/^{9}Be$ ratios of the procedural blanks ranged from $1.6\pm0.4 \times10^{-15}$ to $7.1\pm1.5x10^{-15}$ (mean $2.0 \pm0.5 \times10^{-15}$, n=4). Reported one-sigma uncertainties encompass uncertainties on Purdue AMS measurement, uncertainty on the primary standard, and uncertainties on blank corrections. Table S2-1 presents measurements and erosion rates calculations, with and without quartz enrichment, for soil samples, while Table S2-2 presents measurements and results for river samples, as well as generic metrics for precipitation and slope of the quartz-feeding slopes, used on Fig.13. Figures S2-3 provide enlarged maps of the sampled catchments (relative to Fig.6), and shows the distribution of the rock formations used in Table S2-2 to calculate the % of quartz-bearing lithologies and conduct the weighting of the quartz feeding sources.

Soil/rock Sample [1]	Easting	Northing	Elevation	Quartz used	[^{10}Be]	Shielding factor[2]	P_μ [3]	P_{spal}[3]	Integrated wet bulk density[4]	Erosion Rate[5]	Quartz enrichment factor[4]	Erosion Rate[5]
	(°)	*(°)*	*(m)*	*(g)*	*(10^4 at g^{-1})*		*(at g^{-1} yr^{-1})*	*(at.g^{-1} yr^{-1})*	*(g cm^{-3})*	*m/My*		*m/My*
CLP1 (47-61)r*	-89.621	15.149	2,610	?	41.2 ± 1.2	0.97	0.41	16.6	2.6 ± 0.1	27.6 ± 2.6	1.0 ± 0.0	27.6 ± 2.6
CLP2 (47-62)r*	-89.621	15.149	2,610	?	34.2 ± 1.1	0.97	0.41	16.6	2.6 ± 0.1	32.9 ± 3.1	1.0 ± 0.0	32.9 ± 3.1
SM1 (10-53)s°	-89.687	15.132	2,275	10.60	146.3 ± 13.5	0.92	0.37	13.0	1.6 ± 0.2	11.2 ± 2.1	1.0 ± 0.0	11.2 ± 2.1
SM2 (10-52)s°	-89.687	15.132	2,275	29.38	20.1 ± 4.2	0.92	0.37	13.0	1.6 ± 0.2	78.5± 20.9	1.4 ± 0.3	110 ± 38
SM3 (47-101)s*	-89.645	15.124	1,875	?	13.4 ± 0.6	0.92	0.33	10.1	1.6 ± 0.2	84.1 ± 13.2	1.4 ± 0.3	118 ± 31

Table S2-1. Soil ^{10}Be samples locations, concentrations and environmental parameters. [1] Sample type: s: soil, r: rock. Standard used: *: 07KNSTD, °: KNSTD [2]: combination of topographic obstruction and vegetation shielding. [3] Production rates for neutrons (P_{spal}) and muons (P_μ), calculated using the CRONUS calculator for a polar sea-level ^{10}Be production rate of 5.1 at.g^{-1}.y^{-1} (Balco, Stone et al. 2008), for indicated shielding factor. [4] Quartz enrichment and soil density from published measurements in similarly eroding tropical soils and saprolite (White, Blum et al. 1998, Ferrier, Kirchner et al. 2010, Brocard, Willenbring et al. 2015). [5] CRONUS-calculated using time-dependent ^{10}Be production rate (version 2.3, constants version 2.3, muons version 1.1).

Stream[(1)]	Easting	Northing	Quartz used	[^{10}Be]	Quartz-bearing[(2)] lithologies	A_{Qz} Average elevation[(3)]	A_{Qz} Average Slope	Denudation rate unweighted [(3,5)]	Denudation rate weighted [(5, 6)]	Denudation rate Qz enrichment	Mean annual precipitation
	(°)	*(°)*	*(g)*	*(10^4 at g^{-1})*	*(% total catchment)*	*(m)*	*(°)*	*(m/Myr)*	*(m/Myr)*	*(m/Myr)*	*(mm/y)*
COL (SM)*	-89.644	15.124	32.41	126.84 ± 2.09	CU(100)	2,122	19.3	11.0 ± 1.7	11.0 ± 1.7	15 ± 4	1,420
FRI (SM)*	-89.650	15.109	27.23	24.37 ± 0.66	CU(100)	2,050	24.0	54.3 ± 8.4	54.3 ± 8.4	76 ± 20	1,470
SLO (SM)*	-90.183	14.957	16.85	6.90 ± 0.34	CU(100)	1,892	20.6	163 ± 26	163 ± 26	228 ± 61	1,262
RAN (SM)*	-89.655	15.030	32.56	5.94 ± 0.31	CU(70)	915	31.1	108 ± 10	101 ± 11	142 ± 34	910
SCO (SM)*	-90.101	15.104	28.31	25.84 ± 0.51	CU(81)	2,014	19.3	67.9 ± 6.7	63.9 ± 6.7	90 ± 21	1,250
SIM (SM)*	-90.169	15.112	45.18	21.46 ± 0.90	CU(95)	1,856	18.9	54.4 ±5.8	51.2 ± 5.7	72 ±17	1,220
SBM (SM)*	-90.182	15.079	42.55	27.56 ± 1.12	CU(100)	1,695	19.6	38.0 ± 6.0	38.4 ± 6.0	54 ±14	1,060
MOR (SC)*	-90.183	14.957	17.97	9.82 ± 0.37	CU(81)SR(2)	1,122 (1,213)	20.4	77.7 ± 11.4	73.8 ± 11.3	103 ± 27	790
SALS (SC)*	-90.282	15.061	33.66	21.14 ± 0.48	CU(92)QP(8)	1,330 (1,304)	21.4	39.9 ± 6.2	40.5 ± 6.2	57 ± 15	550
SALI (SC)*	-90.304	15.095	33.05	15.36 ± 0.34	CU(63)QP(25)SR(12)	1,326 (1,243)	20.1	52.7 ± 8.3	55.4 ± 8.4	73 ± 17	590
SMS (SC)°	-90.382	15.025	26.15	19.50 ± 0.38	CU(100)	1,707	18.3	50.2 ± 7.6	50.2 ± 7.6	70 ± 19	510
SMM (SC)*	-90.388	15.062	51.13	21.00 ± 0.32	CU(100)	1,611	20.4	48.7 ± 7.4	48.7 ± 7.4	68 ± 18	490
SMI (SC)°	-90.382	15.148	30.62	20.63 ± 0.11	CU(69)QP(22)SR(9)	1,391 (1,292)	20.3	44.6 ± 7.0	47.3 ± 7.1	69 ± 17	490
SGA (SC)*	-90.406	15.148	43.49	24.67 ± 0.41	CU(43)QP(18)SR(69)	1,172 (1,127)	21.6	30.6 ± 4.8	31.5 ± 4.8	44 ± 12	570
PAT (SC)°	-90.557	15.145	30.09	14.65 ± 0.43	CU(55)SR(45)	1,224 (1,330)	20.9	63.5 ± 9.2	59.7 ± 9.1	84 ± 22	540
ECS (SC)°	-90.559	14.992	15.01	20.84 ± 5.20	CU(91)	1,974	21.9	64.6 ± 20.0	64.6 ± 20.0	90 ± 34	1,140
COT (SC)°	-90.616	14.905	20.29	17.89 ± 0.61	CU(100)	1,637	19.1	61.9 ± 9.6	61.9 ± 9.6	87 ±23	1,120
XEU (SC)°	-90.603	15.058	50.22	7.08 ± 0.28	CU(100)	1,746	25.7	162 ± 25	162 ± 25	227 ± 60	1,090
CUB (SC)*	-90.592	15.123	35.64	8.24 ± 0.27	CU(88)QP(11)	1,432 (1,389)	22.5	103 ± 15	106 ± 16	148 ± 39	990
PAC (SC)°	-90.646	15.155	33.28	10.77 ± 0.28	CU(98)SR(2)	1,211 (1,213)	22.3	80.2 ± 12.1	80.2 ± 12.1	112 ± 29	680
PAS (SC)*	-90.681	15.090	32.13	10.27 ± 0.25	CU(100)	1,947	21.4	112 ± 17	112 ± 17	157 ± 41	1,030
PAE (SC)*	-90.707	15.125	26.01	7.31 ± 0.26	CU(100)	1,779	23.5	146 ± 22	146 ± 22	204 ± 54	840
CHI (SC)*	-90.761	15.158	15.12	28.90 ± 0.75	CU(100)	1,838	21.9	40.0 ± 6.2	40.0 ± 6.2	56 ± 14	560
SAC (SC)*	-90.911	15.153	12.04	17.76 ± 0.54	CU(100)	1,865	23.9	65.8 ± 10.1	65.8 ± 10.1	92 ± 24	1,070
XOL (SC)*	-91.002	15.144	20.95	13.80 ± 0.62	CU(97)QP(3)	1,889 (1,890)	24.7	84.2 ± 13.3	85.4 ± 13.4	113 ± 28	1,410
ACA (SC)°	-90.914	15.206	20.09	12.88 ± 0.38	CU(83)QP(17)	1,635 (1,570)	22.7	81.5 ± 8.5	84.6 ± 12.9	118 ± 31	1,130
CATA (CH)*	-91.130	15.495	55.62	26.56 ± 1.07	SR(18)TS(22)QP(7)	1,944 (1,880)	20.9	44.1 ± 7.1	45.7 ± 7.2	64 ± 17	2,140
CHEL (CH)*	-91.129	15.504	50.65	13.49 ± 0.48	SR(25)TS(20)QP(3)	2,102 (2,027)	23.6	88.6 ± 9.5	92.2 ± 14.3	129 ± 34	2,130
SUM (CH)*	-91.129	15.495	35.37	3.68 ± 0.17	SR(73)TS(14)	1,885 (1,820)	29.0	284 ± 32	294 ± 46	412 ± 109	3,230
IXT (CH)*	-91.089	15.621	44.45	2.99 ± 0.13	SR(93)TS(6)	1,602 (1,720)	29.3	333 ± 34	310 ± 48	434 ± 115	4,090
XAC (CH)*	-91.087	15.619	15.38	4.04 ± 0.35	SR(50)TS(16)QP(2)	2,041 (1,923)	26.9	258 ± 32	274 ± 47	384 ± 105	3,310

Table S2-2. ^{10}Be concentrations and environmental parameters used for the calculation of catchment-wide erosion rates

AQz: area covered by quartz-feeding slopes [1] Sample location: SM: Sierra de las Minas, SC: Sierra de Chuacús, CH: Cuchumatanes Highs. Standard used: *: 07KNSTD, °: KNSTD. [2] Weighting of lithologies in subsequent calculations as follows, normalized to Chuacús (CH): SR. Santa Rosa Fm. (0.4), QP: Quaternary pumice (0.1), Todos Santos Fm. (0.6). [3] Values after applying the quartz-content weighting. [4] Production rates for neutrons (P_{spal}) and muons (P_{μ}), calculated using the CRONUS calculator for a polar sea-level ^{10}Be production rate of 5.1 $at{\cdot}g^{-1}{\cdot}y^{-1}$ (Balco, Stone et al. 2008), for the indicated topographic shielding and vegetation shielding of 7%. [5] Calculated using ground

densities and quartz enrichment factor as for soils in Table S2-1, using the CHRONUS time-depend production rate scheme [6] No weighting according to quartz content for quartz-bearing lithologies.

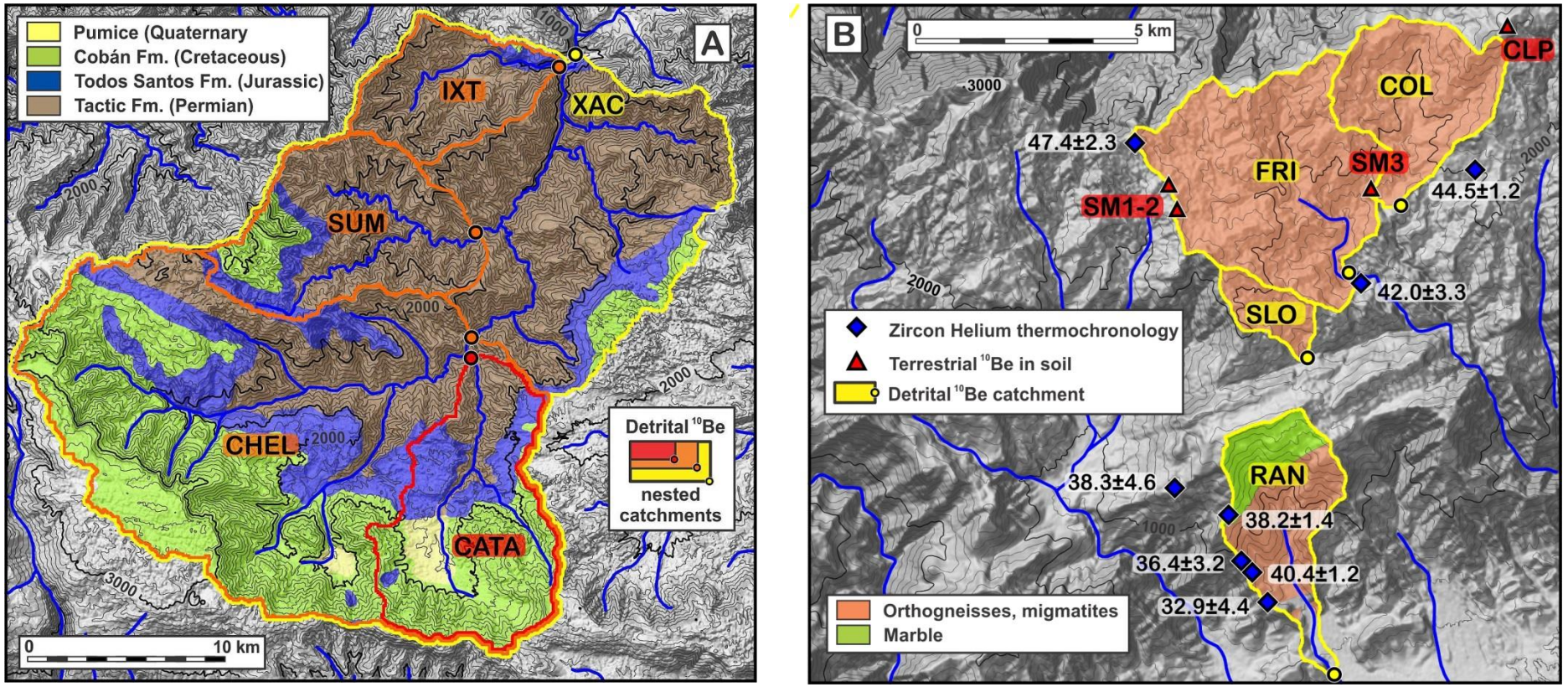

Figure S2-3. Detrital terrestrial cosmogenic ^{10}Be feeding catchment lithology used for the calculation of the effect of quartz concentration on erosion rates. Names of sampled rivers: (a) Altos de Cuchumatanes ; CATA: Catarata, CHEL: Chel, IXT: Ixtahuacan, SUM: Sumalá, XACB: Xacbal), (b) Sierra de las Minas : COL: Colorado, FRI: Frío, RAN: Quebrada Ranchitos/In situ: CLP: Cerro las Palomas, SM: Sierra de las Minas (Zircon data (Simon-Labric, Brocard et al. 2013).

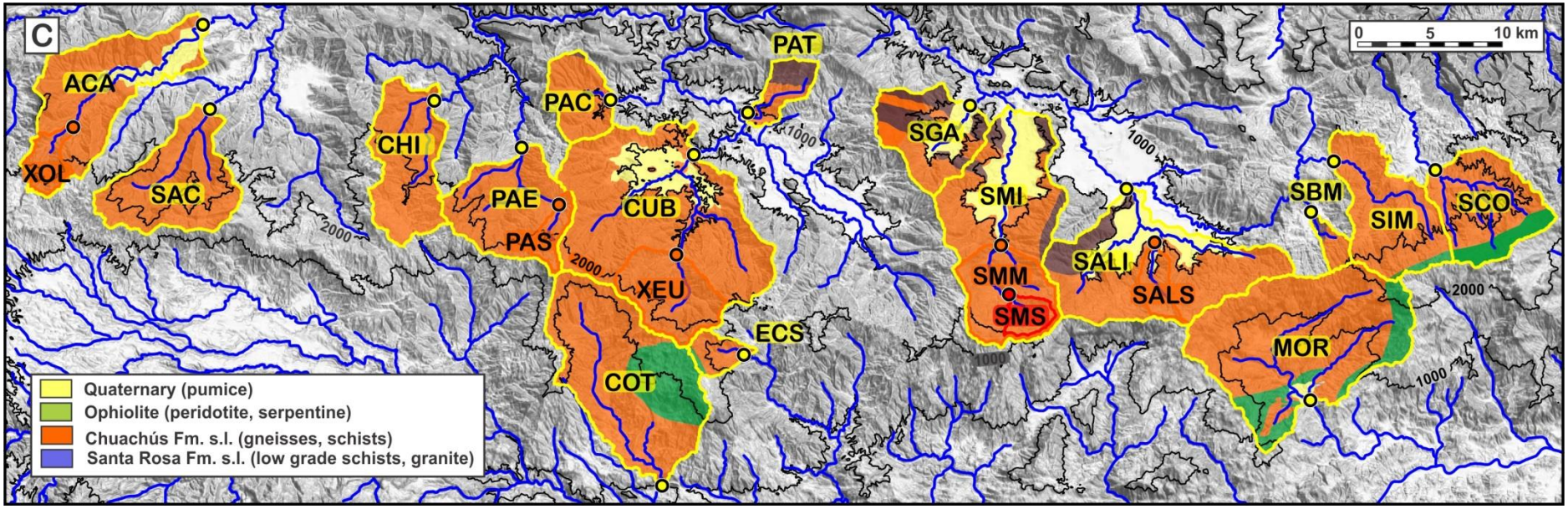

(c) Sierra de Chuacús : ACA: Agua Caliente, CHI:, COT: Cotón, CUB: Cubulco, ECS: El Chol Superior, MOR: Morazán, PAC: Pacani, PAE: Paguoza East, PAS: Paguoza South, PAT: Patixla, SAC: Sacaj, SALI: Salamá Inferior, SALS: Salamá Superior, SBM: Santa Barbara Modern, SCO: Chilasco, SGA: San Gabriel, SIM: San Isidro Modern, SMI: San Miguel Inferior, SMM: San Miguel Midway, SMS: San Miguel Superior, XEU: Xeúl, XOL: Xoljá.

References

Balco, G. (2009). "26Al-10Be exposure age/erosion rate calculators: update from v. 2.1 to v. 2.2." CRONUS Online Calculator, http://hess.ess.washington.edu.

Balco, G., et al. (2008). "A complete and easily accessible means of calculating surface exposure ages or erosion rates from (10)Be and (26)Al measurements." Quaternary Geochronology **3**(3): 174-195.

Brocard, G. Y., et al. (2015). "Effects of a tectonically-triggered wave of incision on riverine exports and soil mineralogy in the Luquillo Mountains of Puerto Rico." Applied Geochemistry **63**: 586-598.

Ferrier, K. L., et al. (2010). "Mineral-specific chemical weathering rates over millennial timescales: Measurements at Rio Icacos, Puerto Rico." Chemical Geology **277**(1-2): 101-114.

Kohl, C. P. and K. Nishiizumi (1992). "CHEMICAL ISOLATION OF QUARTZ FOR MEASUREMENT OF INSITU-PRODUCED COSMOGENIC NUCLIDES." Geochimica et Cosmochimica Acta **56**(9): 3583-3587.

Nishiizumi, K., et al. (2007). "Absolute calibration of 10 Be AMS standards." Nuclear Instruments and Methods in Physics Research Section B: Beam Interactions with Materials and Atoms **258**(2): 403-413.

Simon-Labric, T., et al. (2013). "Preservation of contrasting geothermal gradients across the Caribbean-North America plate boundary (Motagua Fault, Guatemala)." Tectonics **32**(4): 993-1010.

White, A. F., et al. (1998). "Chemical weathering in a tropical watershed, Luquillo Mountains, Puerto Rico: I. Long-term versus short-term weathering fluxes." Geochimica et Cosmochimica Acta **62**(2): 209-226.

Supplement 3. Stream segmentation using LSDTopoTools

We analyzed longitudinal channel profiles using the statistical approach of (Mudd, Attal et al. 2014) implemented using LSDTopoTools, which identifies locations where either erodibility or erosion rates are most likely to change. The software recursively tests possible various combinations of contiguous segments along the selected rivers (Table S3-1), allowing identification of most likely m/n ratio of each river, the statistically most likely number of linearized segments, and their extent (Fig. S3-2). The statistical analysis is performed over after 300 iterations of the segment finding algorithm, and for m/n ratio varying at 0.25 intervals over a range from 0.1 to 0.9. The averaged m/n ratio of the investigated subset of rivers is 0.48 ± 0.11.

Rivers	Best estimate m/n ratio	STD AICc value	Rivers	Best estimate m/n ratio	STD AICc value
Blanco	0.525	130.522	Las Canoas	0.550	31.3209
Cacuj	0.525	209.432	Pagueza	0.500	28.1190
Chibalam-Yerbabuena	0.675	177.548	Quillila-Carchela	0.675	85.8668
ChitapolC	0.625	262.905	Rabinal	0.450	90.7101
ChitapolE	0.500	62.5817	Sacaj	0.450	112.203
Chixoy	0.375	152.800	Salama	0.600	6.53611
Cucul	0.500	65.7579	San Miguel	0.475	160.916
Ekca-Xecam-Chilil	0.350	158.868	Sicache	0.300	412.876
El Molino	0.350	303.865	Xeul	0.550	56.9638
Las Barras	0.325	4.66082			

Table S3-1. Results from statistical method based on the corrected Akaike Information Criterion (AICc) presenting the best estimate m/n ratio for selected rivers in the region. The statistical analysis is running for the main stem and standard deviation of the AICc values are measured after 300 iterations of the segment finding algorithm (Mudd, Attal et al. 2014).

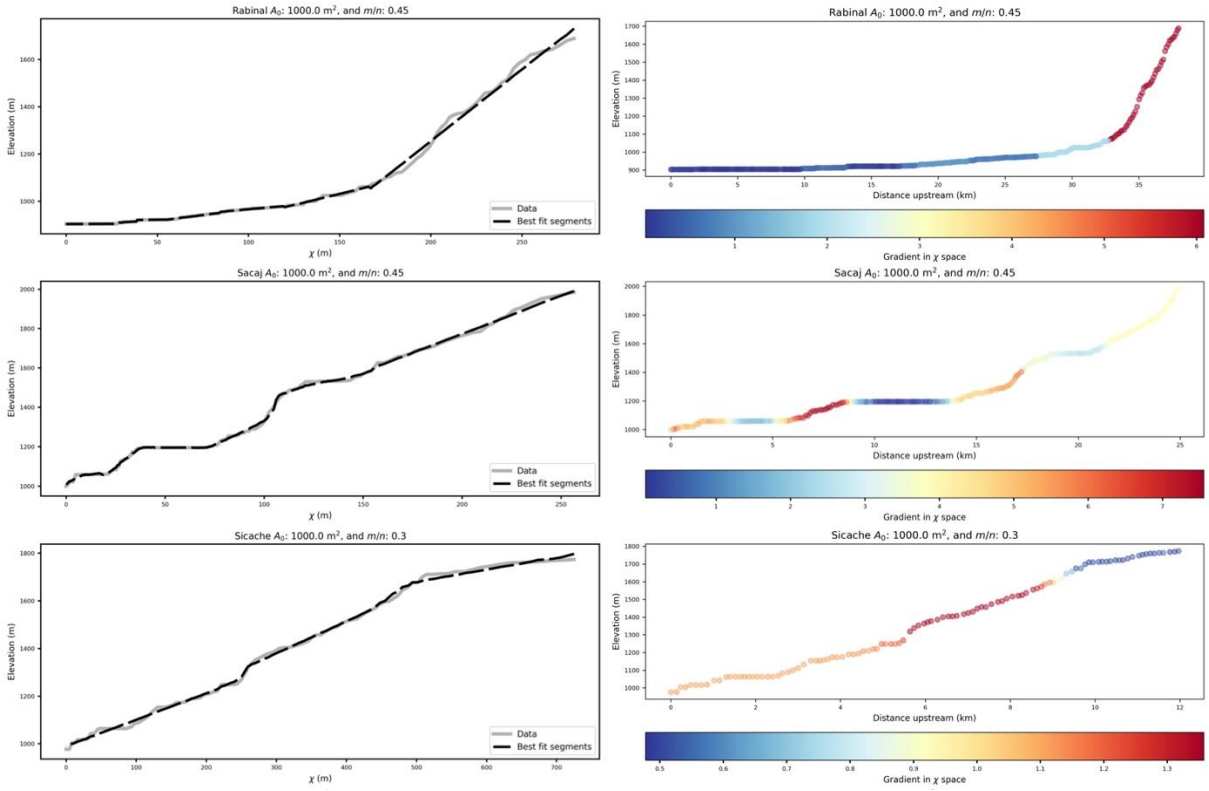

Figure S3-2. Left: segment fitting for three examples of river profiles using the best estimate m/n ratio from the statistical analysis presented in Table SI-31. Right: channel profiles colored by the best fit slope in χ-elevation space. "<atollstatistique.pdf>."

Mudd, S. M., et al. (2014). "A statistical framework to quantify spatial variation in channel gradients using the integral method of channel profile analysis." Journal of Geophysical Research: Earth Surface **119**(2): 138-152.

Supplement 4. Knickpoints and segments regional significance

River profiles were segmented by linearization in chi-space and then divided in successive straight segments. The straight segments and the knickpoints that separate each of them were then classified according to bed type (for straight segments), and knickpoint types. The methodology for segment bed type classification is provided in section 3.5, and for knickpoint classification here, in supplement 4 section 4.1. The classified segments and knickpoints were then projected perpendicular to the strike of the ranges (Figs. S4-2 to S4-7), and along the strike of the AC, SC, and SM ranges (Fig.12a,b,c,d).

4.1. Methodology

River knickpoints were classified into seven knickpoints categories:

1. Lithogenic knickpoints produced by along-stream variations in bedrock erodibility. Downstream increases in erodibility generate concave-up knickpoints, whereas downstream decreases in erodibility generate convex-up knickpoints.
2. Lithogenic knickpoints produced by sudden changes in the streambed orientation relative to the strike and dip/pitch of the dominant structural fabric (bedding, tectonic cleavage, foliation, lineation). Erodibility is usually higher parallel to the structural grain, such that convex knickpoints of this type tend to develop where stream courses veer from subparallel to crosswise to the structural grain. Conversely, concave knickpoints develop where streams become subparallel to the structural grain.
3. Equilibrium tectonic knickpoints, produced by along-stream variations in rock uplift rate. They are convex-up if rock uplift and stream incision increase in the downstream direction, and concave-up otherwise.
4. Alluvial knickpoints, generated by downstream changes in grain size (Johnson, Whipple et al. 2009, Dingle, Sinclair et al. 2016). Convex-up alluvial knickpoints result from an increase in bedload grain-size, usually where steep tributaries inject coarse bedload clasts into the trunk stream. Concave-up knickpoints result from a rapid decrease in grain size, usually by rapid clast sorting, either at the boulder-gravel transition, at the gravel-sand transition, especially at places where bedload grain size distribution is strongly multimodal.
5. Concave-up transitions from detachment-limited to transport-limited river reaches, usually at the apex of alluvial fans (Fig. 8c), and pediments (Fig. 8b). Such transitions appear to nucleate at major lithological boundaries, and to migrate upstream, by backfilling or pedimentation of the lower reaches. They can be viewed as a concave-up equivalent of category 6 (Howard 1997).
6. Upstream migrating convex knickpoints. They separate upstream, slowly incising reaches, from downstream, faster incising reaches. Their location is, in principle, independent of lithological boundaries, and controlled by the laws of knickpoint propagation. In some cases, they consist of two successive convexities: an upper convexity set into a soft shallow substrate (alluvium, saprolite), ahead of a second, usually steeper knickpoint, set into the underlying, harder substrate (Fig. 8d). When reaching junctions, upstream-migrating knickpoints spit and continue their upstream migration along the various tributaries, and clusters of knickpoints, on various drainage branches, can be tracked down to a single origin, either owing to the preservation of terrace tracks formed before the migration of the knickpoints, or because they share similar elevations, or a similar chi value. However, variations in erodibility and erosion efficiency along the various stream branches quickly scatter the elevation and chi values of knickpoints that share a common origin, such that such accordance was rarely found. Some headward-migrating knickpoint in the study area can be tied to local causes, such as river captures and avulsions (Brocard et al., 2012). A few migrating knickpoints have also formed on resistant rock, immediately upstream of erodible substrates, especially below the Maya surface, which stretches with no step, over the resistant and erodible substrates. In this case, the knickpoints may not originate from a distal location, downstream of their current location. Instead, they may have formed locally, at the lithological boundary between erodible and resistant rock, out of faster incision into the most erodible lithology. They are labelled as superimposed transient knickpoints.
7. Miscellaneous knickpoints produced by a variety of other local causes. In the study area, landslides have obstructed some river beds, spurring sedimentary back-filling upstream of the landslide deposits. River profiles are frequently steep where the rivers cross the landslides, or the bedrock of the valley flank opposite to the landslide. Paroxysmal eruptions along the Central American Volcanic Arc have occasionally filled the valleys of Central Guatemala with thick volcanoclastic deposits. The most recent such eruption occurred 84 ky ago, during the formation of the Atitlán caldera (Rose et al., 1987). It led to the deposition of primary and

reworked pumice over thicknesses of 100-200 m in many valleys (Brocard and Morán, 2014; Tobisch, 1986). Rivers have since re-incised these fills down to their pre-eruption levels. One long-lasting effect of this disturbance, however, is the epigenetic re-incision of some river courses, away from the former valley axes, into the former valley flanks, forming knickpoints.

4.2. Results

Table S4-1. River segments and knickpoints (excel file). Table S4-1 provides a list of the river segments, river knickpoints used to characterize the evolution of river profiles in the study area, together with their classification.

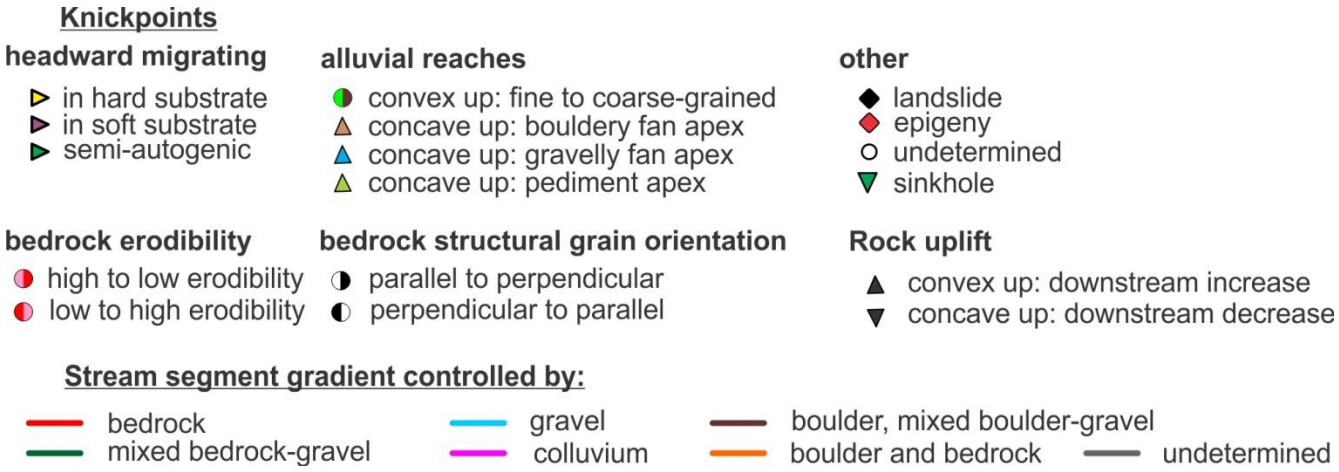

Legend of figures S4-2 to S4-7. Figures S4-2 to S4-7 represent projections of the linearized segment and knickpoints perpendicular to the strikes of the SC, SM, and AC ranges Figure S4-8 represent projections of the linearized segments parallel to the strike of the ranges.

4.3. Analysis of the distribution of knickpoints in the SC, SM and AC ranges

Distribution of concave-up knickpoints

Concave-up knickpoints fringe the southern base of the SM-SC range (Fig. 12-a1). They are located at the apex of broad, alluvial fans, upstream of the transition between resistant basement rocks upstream, and more erodible ophiolitic mélanges and Eocene red beds downstream, along the Motagua valley. They also dot the northern base of the SM range, at the apex of alluvial fans that grade to the fill of the Lake Izabal basin. Along the northern base of the SC range, concave-up knickpoints are located farther up within the range than along the northern flank of the SM range. They are separated from the range-parallel Chixóy River by broad pediments. These pediments are extensively covered by pumice emplaced during the last paroxysmal eruption of the Atitlán caldera 84 ky ago (Los Chocoyós pumice). Most rivers have incised this pumice down to pre-eruption levels, such that they rest directly on the underlying basement. In the AC range, most concave-up knickpoints are located immediately downstream of the Ixcán reverse fault which marks the front of the AC range to the NE.

Distribution of lithogenic knickpoints

Lithogenic knickpoints produced by large changes in bedrock resistance or by changes in the orientation of the streams with respect to the bedrock fabric are common halfway down mountain flanks. They tend to be generated by more subtle changes in bedrock resistance high up the mountain flanks, where crystalline rocks weather to sand and gravel, than farther downstream, where streambeds are armoured by immobile boulders or large cobbles (e.g. Fig. 8c). The absence of boulder armouring makes upper reaches more sensitive to bedrock erodibility variations (Johnson, Whipple et al. 2009). Similar higher sensitivity at

high elevation is also found high up the AC range, where limestones and sandstones deliver little sediment to the streams.

Distribution and origin of tectonic knickpoints

The majority of tectonic knickpoints are located along the southern flank of the AC range, within a few hundreds of meters from the active trace of the Polochic fault, in the vicinity of pressure ridges, and within 4 km of the fault along narrow transtensional corridors (Authemayou, Brocard et al. 2012). No tectonic knickpoints are found along the southern flank of the releasing bend of Lake Izabal, indicating that the southern side of the basin is not bound by large active faults, in agreement with the sedimentary architecture of the basin (Carballo-Hernandez, Banks et al. 1988, Bartole, Lodolo et al. 2019).

The overall downstream steepening of river profiles along the northern flank of the AC range over the hanging wall of the Ixcán transpressional fault may reflect increasing rock uplift rates within 20 km of the fault. This steepening is progressive, but it is at places associated with changes in bedrock lithology, and sharper changes in streambed type. The knickpoints associated to these lithological changes therefore classified as composite, tectonic-lithogenic knickpoints (Fig. 12b2). They could as well mark the front of a wave of accelerate incision, triggered by an acceleration of differential tectonic uplift (Whittaker, Cowie et al. 2007) across the Ixcán fault, or simply an overall steepening due to increasing uplift rate in the downstream direction, at dynamic equilibrium (Kirby and Whipple 2001).

No large tectonic separation of the Maya surface is observed along the NW flank of the AC range, where the Maya surface rises regularly from the Central Depression of Chiapas a kink fold (Fig.2 and 4). The mid-elevation migrating knickpoints present along the NW flank could have been produced by river steepening, without nucleating over a specific tectonic dislocation (Willenbring, Gasparini et al. 2013). Similarly, river steepening could account for the presence of two successive migrating knickpoints along the paleovalley of Quilén Novillo-Chancol, on the southern side of the range (Fig.8a).

Distribution of ambiguous clusters of mixed origin

A series of knickpoints is found along the base of the SC range, downstream of the pedimented valley floors (Fig. 8b). They could be lithogenic knickpoints, as they coincide with lithological changes. The presence of lithogenic knickpoints at low elevation is rather uncommon, and suggests some recovery of the sensitivity of the stream beds to lithological changes. This could result from the trapping or/and comminution of the coarsest bedload (Johnson, Whipple et al. 2009) on the pediments, upstream of these knickpoints. They are restricted to the Chixóy Basin and are not observed along the northern flank of the SM range (Fig. 12b2). They could therefore also result from the propagation of a wave of incision restricted to the Chixóy River drainage, as the Chixóy River itself hosts a potentially migrating knickpoint farther upstream (downstream of Sacapulas). The Chixóy River knickpoint, however, could also be lithogenic, or even result from uplift in the footwall of a normal fault near Sacapulas. However, this later fault is probably no longer active, as its scarp shows no indication of recent slip. The most likely, or complementary explanation to the lithogenic cause, is that these knickpoints have a tectonic origin. The Chixóy River established its range-parallel course between the AC and SC range at the lowest point in the saddle between the two ranges at 7 Ma (Brocard et al., 2011). Today, however, the axis of this saddle is located 6-8 km farther south, suggesting that the saddle migrated as a result of the uplift of the AC range. The knickpoints located very near the Chixóy River could therefore most likely mark the southern extend of uplift related to the rise of the AC range.

Distribution and origin of migrating knickpoints

Among the population of migrating knickpoints, a few are associated with well-identified and dated river diversions (S3-1 to S3-3, Fig. 12a2) that occurred during the Quaternary (Brocard, Willenbring et al. 2012). They sparked the incision of 500 to 1,000 m-deep canyons, spearheaded by prominent migrating knickpoints.

Most headward-migrating knickpoints are located along the margins of upland low-relief surface remnants (Fig. 12 a1 and a2; Fig. 8d). They are seemingly less common in the AC range than in the SC and SM ranges, merely because the uplands of the AC range are karstified and lack an organized drainage and its associated knickpoints at their surface.

A cluster of migrating knickpoints along the southern flank of the SC range, in the upper part of the Motagua valley, coincides with the elevation of tertiary ignimbrites in the region of Pachalum (Fig. 12a1). These migrating knickpoints lie at the head of valleys incised into degraded, low-relief pediments that are, at places, covered by ignimbrites (Fig. 12a1). These ignimbrites are not dated, but hang above the Motagua River at about the same elevation as the El Jute basalt. They are therefore most likely late Miocene in age, an age consistent with the age of the ignimbrites that fill the paleovalleys farther north (Brocard et al., 2011), as well as farther south in the Central American volcanic arc (Jordan et al., 2007). The downstream convergence of these ignimbrites with the Motagua River, and the steepening of the Motagua River upstream of the convergence point together suggest that renewed incision is taking place in the headwaters of the Motagua River. It is probably driven by uplift of the Central American Volcanic Arc. The extent and amplitude of this uplift is difficult to track farther upstream the Motagua valley, because the course of the Motagua River becomes increasingly chocked with pyroclastic deposits emplaced during caldera-forming eruptions along the volcanic arc (Wunderman and Rose, 1984). The last such eruption disrupted the course of the Motagua River 84 ka ago. Primary pumice flows produced during this eruption deposited 100-200 m of pumice along the base of the SC range (Fig.12a), and several tens of meters of reworked pumice farther downstream (Tobisch, 1986). This short-lived event did not generate knickpoints along the tributaries of the Motagua River, because most streams rapidly recovered their pre-eruption profiles. The pumice, however, altered the upper course of the Motagua River, such that the river has since epigenetically incised in harder volcanic substrates, generating knickpoints. At the other, downstream end of the Motagua River, sea level variations had no noticeable impact upstream of Los Amates, on the studied reaches of the Motagua River, (LA, Fig. 12a).

An ill-defined cluster of migrating knickpoints is found along the southern flank of the AC range. Its extent and origin is obscured by the presence of many tectonic disruptions along the Polochic fault. Another cluster of headward-migrating knickpoints is present halfway down the northwest flank of the AC range, along rivers draining toward the central depression of Chiapas (Fig. 12). The horizontal bedding of the bedrock makes it difficult to separate headward-migrating knickpoints from lithogenic-knickpoints in this part of the range, because they generate similar topographic landforms.

Another cluster half way down the northern flank of the SC range affects the drainage of the Chixóy River catchment, but not the drainage of the Polochic-Panimaquito, along the northern flank of the SM range. Its origin is discussed in section 5.3.2.

Authemayou, C., et al. (2012). "Quaternary seismo-tectonic activity of the Polochic Fault, Guatemala." Journal of Geophysical Research-Solid Earth **117**.

Bartole, R., et al. (2019). "Sedimentary architecture, structural setting, and Late Cenozoic depocentre migration of an asymmetric transtensional basin: Lake Izabal, eastern Guatemala." Tectonophysics **750**: 419-433.

Brocard, G., et al. (2012). "Rate and processes of river network rearrangement during incipient faulting: The case of the cahabon river, guatemala." American Journal of Science **312**(5): 449-507.

Carballo-Hernandez, M., et al. (1988). Cuenca Amatique, Guatemala: Una Cuenca Transtencional al Sur del Limite de Placas NorteAmericana–Caribe. Paper Presented at Congreso Geologico Chileno, Soc. Geol. Chile, Santiago.

Dingle, E. H., et al. (2016). "Subsidence control on river morphology and grain size in the Ganga Plain." American Journal of Science **316**(8): 778-812.

Howard, A. D. (1997). "Badland morphology and evolution: Interpretation using a simulation model." Earth Surface Processes and Landforms: The Journal of the British Geomorphological Group **22**(3): 211-227.

Johnson, J. P., et al. (2009). "Transport slopes, sediment cover, and bedrock channel incision in the Henry Mountains, Utah." Journal of Geophysical Research: Earth Surface **114**(F2).

Kirby, E. and K. Whipple (2001). "Quantifying differential rock-uplift rates via stream profile analysis." Geology **29**(5): 415.

Whittaker, A. C., et al. (2007). "Contrasting transient and steady-state rivers crossing active normal faults: new field observations from the Central Apennines, Italy." Basin Research **19**(4): 529-556.

Willenbring, J. K., et al. (2013). "What does a mean mean? The temporal evolution of detrital cosmogenic denudation rates in a transient landscape." Geology **41**(12): 1215-1218.

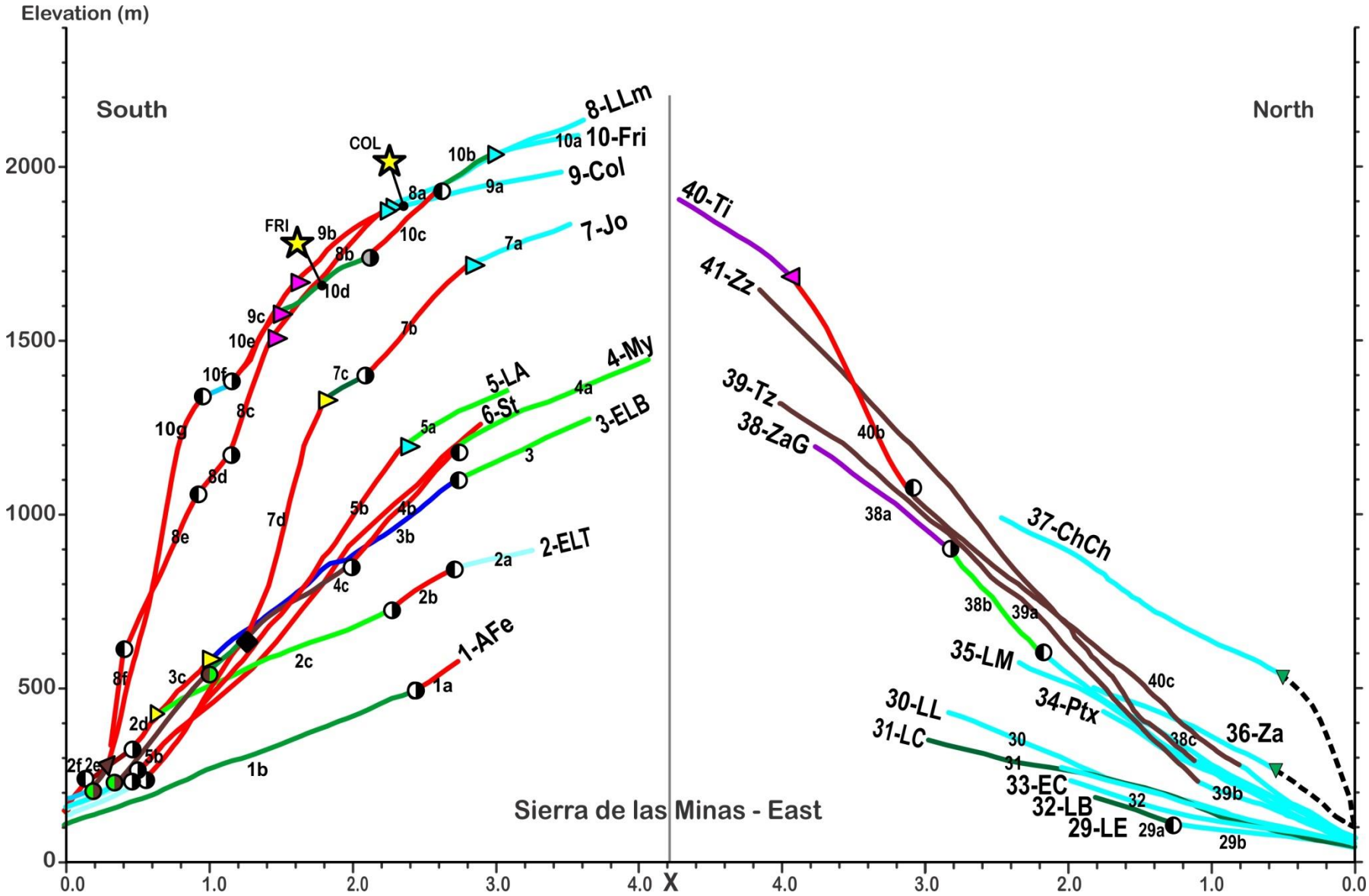

Figure S4-2. χ-plot of the rivers that drain the northern and southern flanks of the eastern SM range (Sierra de las Minas).
River names: Southern flank: 1-AFe: Agua Fría east; 2-ELT: El Lobo-Tinto; 3- ELB: El Lobo-Blanco; 4-My: Mayuelas, 5-LA: Los Achiotes, 6-St: Santiago, 7-Jo: Jones, 8-LLm: La Lima, 9-Col: Colorado, 10-Fri: Agua Fría. Northern flank: 29-LE: Los Espinos, 30-LL: Los Limones, 31-LC: Las Cañas, 32-LB: Las Balandras, 33-EC: El Chapín, 34-Ptx: Pataxte, 35-LM: Las Minas, 36-Za: Zarquito, 37-ChCh: river on carbonates ending in sinkhole, 38-ZaG: Zarco Grande, 39-Tz: Tze, 40-Ti: Tinajas, 41-Zz: Zarzaparillas. Yellow stars: sampling sites for detrital ^{10}Be erosion rate measurements.

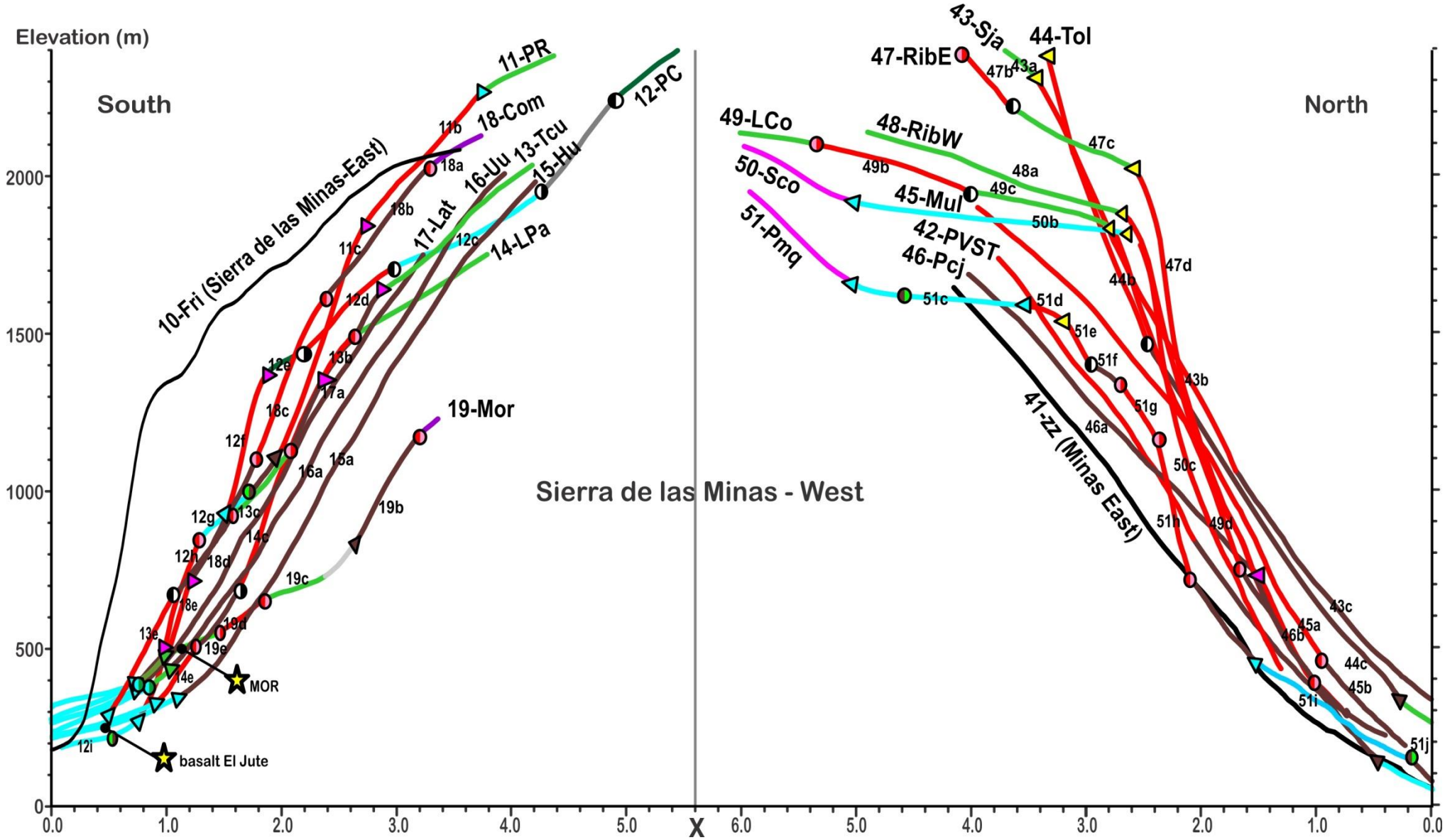

Figure S4-3. χ- plot of the rivers that drain the northern and southern flanks of the western part of the SM range (Sierra de las Minas).
River names: Southern flank: 11-PE: Pasabien Repollal, 12-PC: Pasabien-Chorro, 13-Tcu: Teculutan, 14-LPa: La Palmilla, 15-Hu: Huijo, 16-Uu: Uyus, 17-Lat: Lato, 18-Com: Comaja, 19-Mor: Morazán. Northern flank: 41-Zz: Zarzaparilla, 42-PVST: Pueblo Viejo-Santo Toribio, 43-Sja: Samilija, 44-Tol: Toila, 45-Mul, Mululjá, 46-Pcj: Pancajoc, 47-RibE: Ribaco east, 48-RibW: Ribaco west, 49-LCo: La Concepción, 50-Sco: Chilasco, 51-Pmq: Panimaquito. Yellow stars: sampling sites for detrital ^{10}Be erosion rate measurements.

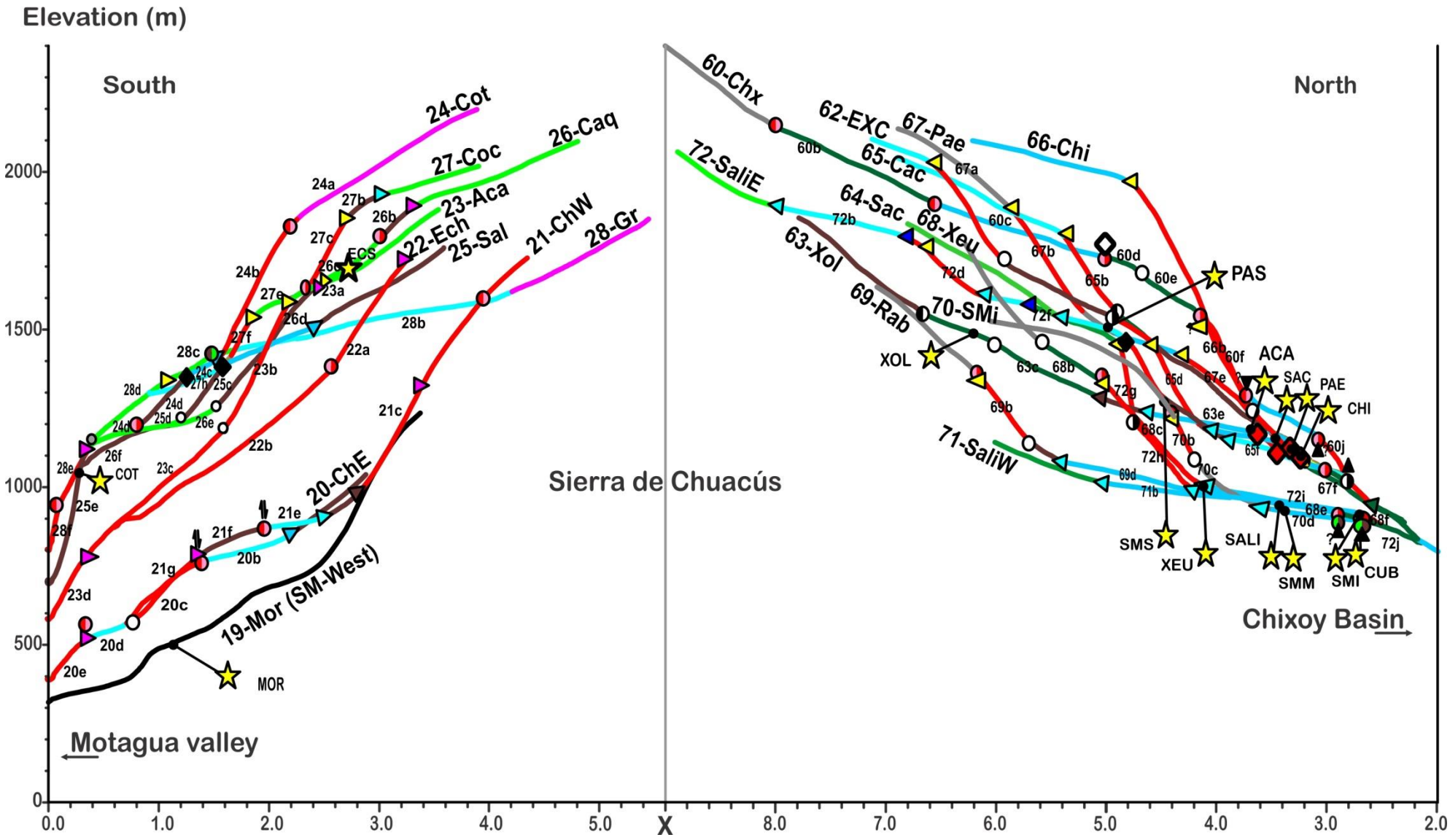

Figure S4-4. χ-plot of the rivers that drain the northern and southern flanks of the SC range (Sierra de Chuacús).
Stream names: Southern flank: 20-ChE: Chuacús East, 21-ChW: Chuacús west, 22-ECh: El Chol, 23-Aca: Agua Caliente, 24-Cot: Cotón, 25-Sal: Saltán, 26-Caq: Caquíl, 27- Coc: Cocol, 28-Gr: Grande. Northern flank: 72-SaliE: Salamá East, 71-SaliW: Salamá West, 70-SMi: San Miguel, 69-Rab: Rabinal, 68-Xeu: Xeul, 67-Pae: Pagueza, 66-Chi: Chiabalam-Yerbabuena, 65-Cac: Cacúj, 64-Sac: Sacaj, 63-Xol: Xoljá, 62-EXC: Ekca-Xecam-Chilil, 61: Cuc: Cucul, 60-Chx: Chixóy. Yellow stars: sampling sites for detrital ^{10}Be erosion rate measurements.

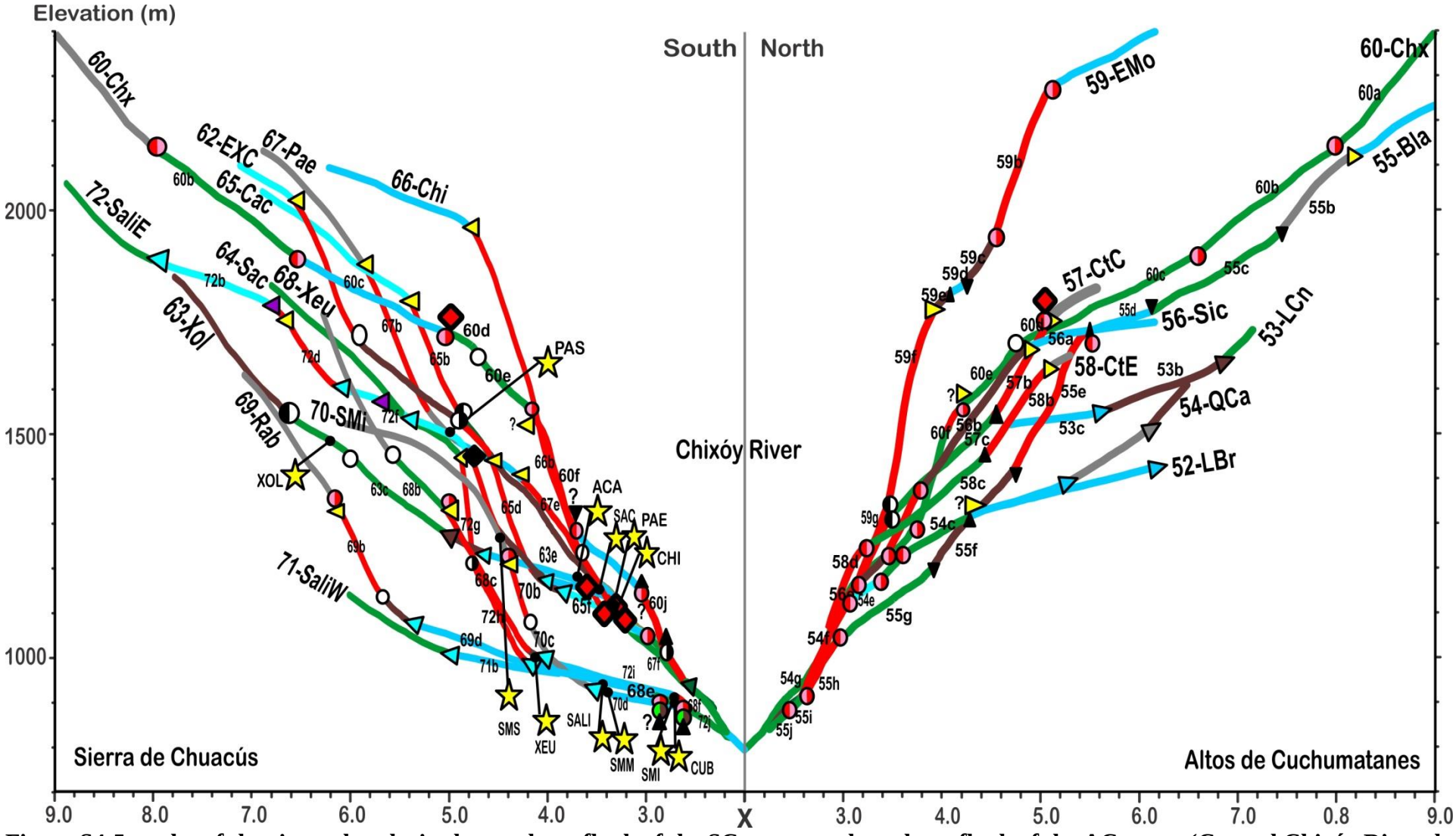

Figure S4-5. χ-plot of the rivers that drain the northern flank of the SC range, and southern flank of the AC range (Central Chixóy River drainage). River names: Southern flank: 72-SaliE: Salamá East, 71-SaliW: Salamá West, 70-SMi: San Miguel, 69-Rab: Rabinal, 68-Xeu: Xeul, 67-Pae: Pagueza, 66-Chi: Chiabalam-Yerbabuena, 65-Cac: Cacúj, 64-Sac: Sacaj, 63-Xol: Xoljá, 62-EXC: Ekca-Xecam-Chilil, 61: Cuc: Cucul, 60-Chx: Chixóy. Northern flank: 52-LBr: Las Barras, 53-LCa: Las Canoas, 54-QCa: Quililá-Carchela, 55-Bla: Blanco, 56-Sic: Sicaché, 57-Ctc: Chitapol Centre, 58: CtE: Chitapol East, 59-EMo: El Molino 60-Chx: Chixóy. Yellow stars: sampling sites for detrital ^{10}Be erosion rate measurements.

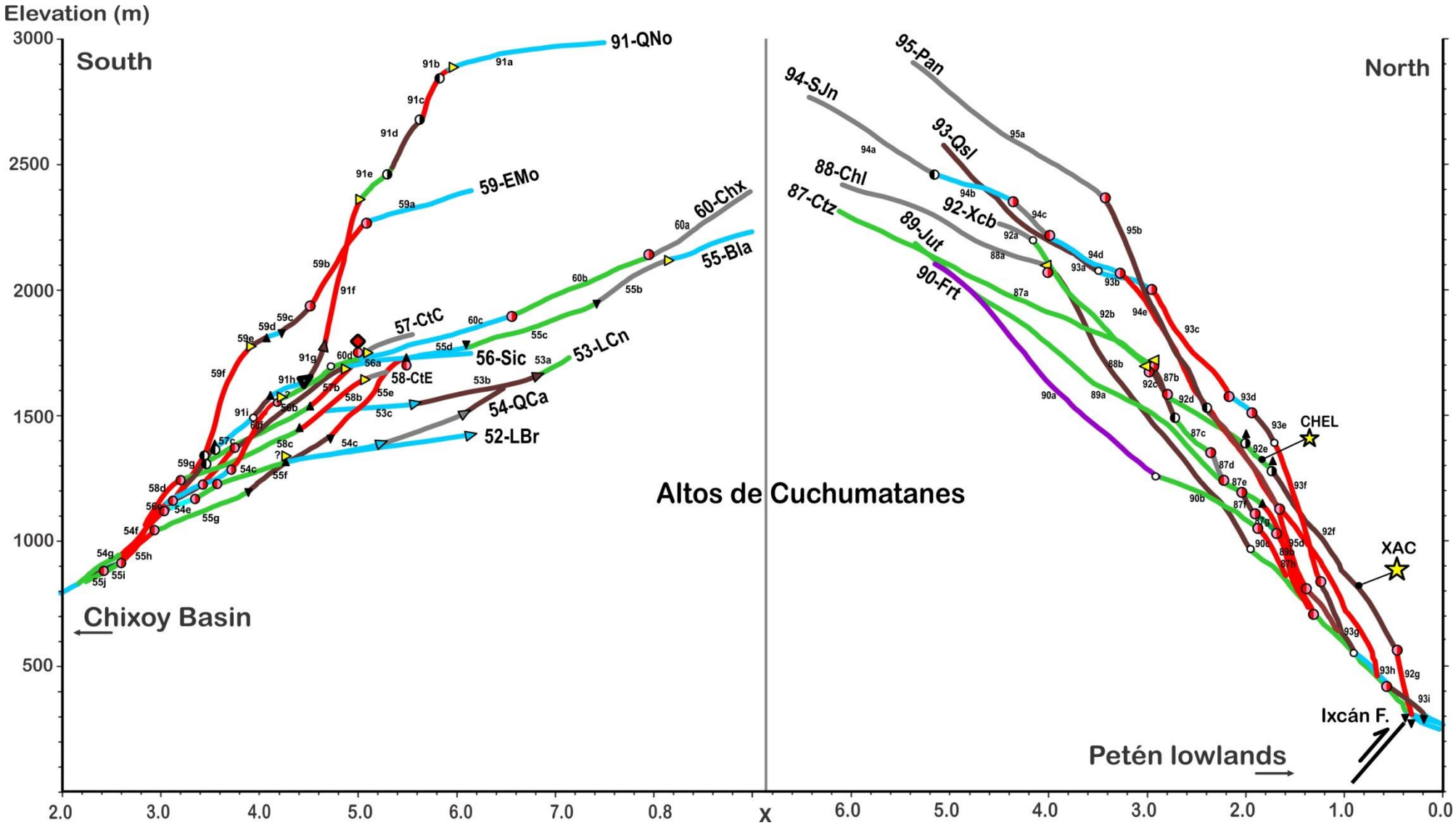

Figure S4-6. χ-plot of the rivers that drain the southern and northeastern flanks of the AC range (Altos de Cuchumatanes)
River names: Southern flank: 52-LBr: Las Barras, 53-LCa: Las Canoas, 54-QCa: Quililá-Carchela, 55-Bla: Blanco, 56-Sic: Sicaché, 57-Ctc: Chitapol Centre, 58: CtE: Chitapol East, 59-EMo: El Molino 60-Chx: Chixóy.
Northern flank: 87-Ctz: Cotzal, 88-Chl: Chel, 89-Jut: El Jute, 90-Frt: unnamed frontal stream, 91- QNo: Quilén Novillo, 92- Xcb: Xacbal, 93- Qsl: Quisil, 94-SJn: San Juan, 95- Pan: Panila. Yellow stars: sampling sites for detrital ^{10}Be erosion rate measurements.

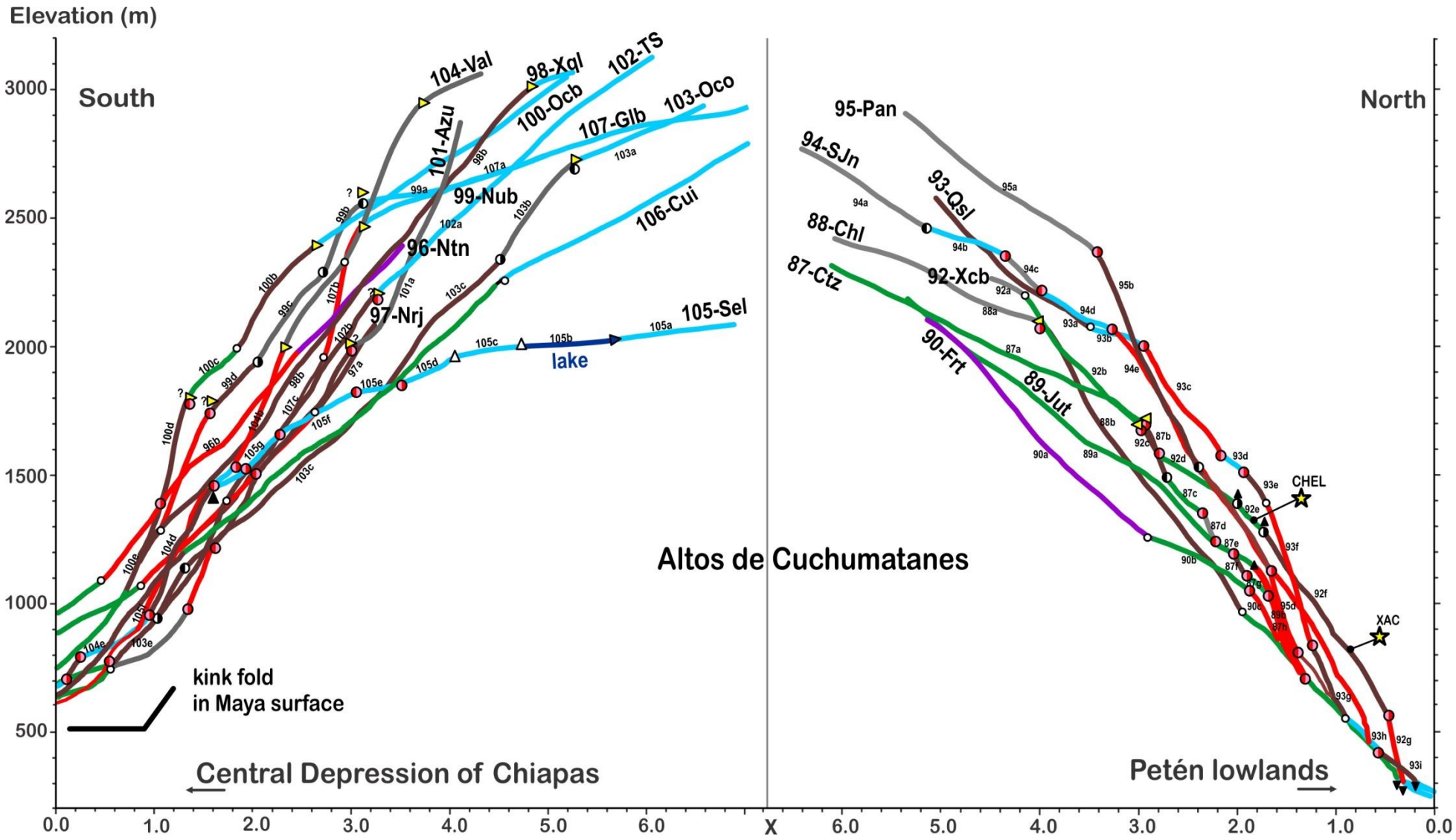

Figure S4-7. χ-plot of the rivers that drainage the northwestern and northeastern flanks of the AC range (Altos de Cuchumatanes).
River names: Northern flank: 87-Ctz: Cotzal, 88-Chl: Chel, 89-Jut: El Jute, 90-Frt: unnamed frontal stream, 91- QNo: Quilén Novillo, 92- Xcb: Xacbal, 93-Qsl: Quisil, 94-SJn: San Juan, 95- Pan: Panila.
Eastern flank: 96-Ntn: Nenton, 97- Nrj: Naranjo, 98- Xql: Xoquil, 99-Nub: Nubila, 100-Ocb: Ochebal-Catarina, 101-Azu: Azul, 102-TS: Todos Santos, 103-Oco: Ocho, 104-Val: Valparaiso, 105-Sel: Selegua, 106-Cui: Cuilco. Yellow stars: sampling sites for detrital ^{10}Be erosion rate measurements.